

<https://doi.org/10.1038/s43247-026-03190-y>

European coastal deformation drives unequal exposure to climate hazards

Check for updates

Huilin Chen¹, Chisheng Wang¹ , Jose Fernandez², Huawei Hou¹, Ling Chang³ & Qingquan Li¹

Climate change and land subsidence are altering relative sea levels and compounding risks across European coasts, yet vulnerability assessments at this scale remain limited. Here we integrate 100-meter Interferometric Synthetic Aperture Radar measurements (2019–2023) with land-cover, population, and socioeconomic data to assess physical and social dimensions of coastal exposure. Northern Europe shows uplift exceeding 5 mm per year, while subsidence is prevalent in Mediterranean regions. Wetlands experience the largest downward motion (2.3 ± 3.1 mm per year) despite covering a small share of coastal areas. Under a middle-of-the-road climate scenario for 2050, roughly 94,000 square kilometers of coastal land, nearly 25 million residents, and 8 million buildings may face inundation. Vulnerability is disproportionately elevated among older adults, marginalized populations, and economically constrained regions facing heightened exposure yet limited adaptive capacity. These findings provide a scientific basis for directing adaptation resources where physical hazards and social inequalities converge.

Coastal areas hold a globally important position due to their unique geographical location, abundant natural resources, and important ecological functions. These regions are home to many major cities and population centers in the world, with approximately 70% of the world's megacities (>10 million people) located within 60 kilometers of the coast, contributing 50% of the world's GDP^{1–3}. As an intermediate region connecting land and marine habitats, coastal areas are widely regarded as one of the most productive and respected ecosystems on Earth^{4–6}. Meanwhile, coastal areas are highly susceptible to the impacts of global change, with environmental changes and other types of stressors originating from human development affecting their vulnerability^{7,8}. In particular, climate change exacerbates risks through multiple pathways, including the increasing frequency of extreme storm events, the degradation of coastal ecosystems, and sea level rise (SLR)^{9–11}. Against this backdrop, land subsidence and SLR, observed over the past century, pose growing threats to coastal areas, whose vulnerability continues to intensify under ongoing climate change and human activities^{12,13}.

Numerous coastal areas worldwide are already under intensifying pressure from relative sea-level rise. This risk is further exacerbated in cities undergoing severe land subsidence—such as Jakarta, Tianjin, Ho Chi Minh City, Venice, and New Orleans—where groundwater over-extraction and soft soil compaction greatly heighten their vulnerability

to inundation^{14–19}. By 2050, global economic assets exposed to flooding are projected to increase substantially²⁰. By 2070, the population at risk of coastal flooding is expected to rise notably due to the combined effects of land subsidence, SLR, and urbanization^{21–23}. The interaction between climate-induced SLR and vertical land motion (VLM) has altered relative sea levels across the world's coastal regions²⁴. Subsidence also amplifies the impacts of other coastal hazards, such as tsunamis and storm surges, by lowering ground levels and increasing the depth and extent of inundation^{25,26}. In low-elevation coastal zones, subsidence exacerbates seawater intrusion and amplifies tidal fluctuations, leading to soil and groundwater salinization, which diminishes land productivity and threatens the sustainability of freshwater resources^{27,28}. Furthermore, the combined effects of seawater intrusion and tidal fluctuations impose long-term corrosive stress on coastal infrastructure, seriously compromising the durability and functionality of critical facilities, including transportation, energy, and communication systems²⁹. Notably, subsidence accelerates wetland degradation and disrupts sediment replenishment, impairing wetlands' ability to maintain essential ecological functions, such as water purification, flood regulation, and carbon storage^{30–33}. These processes illustrate how land subsidence and SLR rise interact to generate compound and cascading impacts on both natural ecosystems and human systems. When such interactions accumulate, they create highly complex risk environments.

¹Ministry of Natural Resources (MNR) Key Laboratory for Geo-Environmental Monitoring of Great Bay Area & Guangdong Key Laboratory of Urban Informatics & Shenzhen Key Laboratory of Spatial Smart Sensing and Services, School of Architecture & Urban Planning, Shenzhen University, Shenzhen, China. ²Institute of Geosciences (IGEO), CSIC-UCM, Madrid, Spain. ³Faculty of Geo-Information Science and Earth Observation, University of Twente, Enschede, The Netherlands.

e-mail: wangchisheng@szu.edu.cn

Table 1 | Fluctuation characteristics of coastal VLM rates in Europe between consecutive observation periods (unit: mm per year)

Region	>0.5	-0.5 ≤ change ≤ 0.5	<-0.5
Atlantic	22%	53%	25%
Med and Black Sea	14%	71%	15%
Europe	19%	59%	22%

Med and Black Sea refer to the Mediterranean and Black Sea region.

In this regard, Europe's coastal regions provide a representative case: their exposure to compound threats is further shaped by diverse geological dynamics—including deglaciation, tectono-sedimentary evolution, and volcanic activity—which produce intricate VLM patterns and make the continent a valuable natural laboratory for coastal research^{34–36}.

Building on this global perspective, the European coastal zone exemplifies such compound risks, while also exhibiting marked spatial variability in VLM, characterized by regional contrasts between uplift and subsidence. In northern Europe, represented by the Scandinavian Peninsula, the coastline was primarily shaped by glacial erosion during the last glacial maximum. Following the retreat of the ice sheet, the crust experienced an isostatic rebound due to unloading, and the land has continued to rise at an average annual rate of 1–10 millimeters, resulting in a marked decrease in relative sea level in the region (locally accumulated over 300 meters)³⁷. In contrast, the central and southern parts of the European coastal zone are mostly vast alluvial plains, while the Mediterranean coast of southern Europe is located in the collision zone between the African Plate and the Eurasian Plate, with frequent tectonic activity and active seismic and volcanic phenomena^{38–40}. Therefore, in areas such as the Netherlands, the Po River Delta in Italy, and the northern coast of Germany, due to geological conditions and human activities, hotspots of land subsidence in Europe have been focused on^{41–44}. There are extensive investigations and records of local subsidence areas along the European coast in existing research, but comprehensive studies that consider the European coastal zone as a whole system are still lacking.

This gap has motivated increasing reliance on advanced observation technologies. In recent decades, the development of satellite remote sensing monitoring, elevation measurement, and tide gauge analysis technologies has provided extensive data support for the spatiotemporal analysis of coastal subsidence phenomena^{45–47}. Although considerable progress has been made in existing research on land subsidence in European coastal areas, these studies mainly focus on local hotspot regions (such as the Po River Delta and western Netherlands), lacking systematic spatial heterogeneity analysis covering the entire European coastal zone, making climate adaptation among countries more difficult to coordinate. More importantly, from an equity perspective, the risks associated with land subsidence are likely to be distributed highly unevenly across different social groups. At present, systematic understanding at the European scale of how the spatial patterns of ground subsidence interact with land cover and socio-economic factors to shape social vulnerability remains limited. This knowledge gap constrains progress toward equitable adaptation goals that aim to ensure that vulnerable populations and regions are not disproportionately left behind^{48,49}. To address these challenges, a multi-source data fusion analysis framework was developed. Building on the continental VLM mapping provided by European Ground Motion Service (EGMS), the framework integrates land cover, socio-economic, and population data to enable a critical transition: transforming physical subsidence patterns in coastal zones into spatially explicit assessments of socio-economic vulnerability⁵⁰. Such an approach advances the understanding of the socio-economic implications of coastal subsidence across Europe and strengthens the evidence base for promoting equitable coastal risk governance.

Results and discussion

Patterns and regional characteristics of vertical land motion across European coastal zones

Natural factors, such as crustal structure and glacial isostatic adjustment, as well as human activities including groundwater extraction, can influence the observed VLM signals. To evaluate the stability of EGMS data in representing VLM rates, a conservative threshold of ± 0.5 mm per year was adopted as a reference for identifying fluctuations⁵¹. A comparison of VLM data for two consecutive periods (2018–2022 and 2019–2023) across the European coastal zone, covering approximately 65 million pixels (corresponding to the 100 m resolution grid covering the European coastal zone), indicates that the vast majority of coastal areas exhibit highly consistent VLM rates (Table 1): about 59% of the pixels show variations within ± 0.5 mm per year, highlighting the overall stability of the dataset. Specifically, around 53% of the Atlantic coastline shows no evident change in VLM rates, while the proportion is as high as 71% along the Mediterranean and Black Sea coasts, further underscoring the reliability of the data in these regions. Although roughly 27% of the Atlantic coastline displays VLM rate changes exceeding 1 mm per year (See Supplementary Table 1), revealing genuine land motion differences, the EGMS data overall remain consistent across different coastal regions. In particular, in areas such as the Mediterranean and Black Sea coasts—where tectonic activity is relatively weak, glacial isostatic adjustment effects are limited, and human activities are more effectively regulated—VLM observations appear more stable, demonstrating the robustness and regional applicability of the dataset^{52,53}. In summary, the high stability of EGMS data across different temporal windows provides a reliable basis for its application in monitoring coastal ground motion.

According to VLM observation data from the past 5 years (2018–2023, Fig. 1), the coastal zones of Sweden and Finland in Northern Europe have experienced notable ground uplift, with an average rate exceeding 5 mm per year. One of the primary geodynamic processes driving this uplift is glacial isostatic adjustment^{54,55}. Similarly, glacial isostatic adjustment has also induced land uplift in the coastal zones of Norway and Estonia, although the rates are more moderate, with annual averages remaining below 2 mm per year^{56,57}. In contrast, Iceland, as a typical volcanic island nation located on the mid-Atlantic ridge, exhibits highly active geological and geothermal activities, resulting in localized crustal uplift or subsidence, while glacial retreat further promotes crustal uplift by reducing surface loading, leading to VLM values characterized by a relatively even distribution between subsidence and uplift^{58–60}. Meanwhile, the VLM values in Latvia and Denmark exhibit a relatively concentrated distribution, with the median close to 0 mm per year, indicating that VLM in these areas is relatively stable and crustal activity is generally in equilibrium compared to other regions.

Moving southward from northern Europe, the continent-wide pattern of VLM reveals a pronounced north–south gradient, with coastal uplift prevailing across Northern Europe, while subsidence dominates along the Mediterranean and Black Sea coasts (Fig. 2). According to high-precision monitoring data from the EGMS, four major coastal subsidence hotspots have been identified (See Supplementary Fig. 1): the northern coast of the Netherlands, Thessaloniki in Greece, the Po River Delta in Italy, and Schiavonea in Italy. Notably, Schiavonea represents a subsidence hotspot revealed by EGMS data, which enhances the understanding of subsidence patterns along European coastlines and provides additional scientific insights into regional crustal movements⁵⁰. Along the Atlantic coast of western Europe, the average VLM rates are generally below 2 mm per year; low-lying countries, such as the Netherlands and Belgium, face particularly pronounced coastal subsidence, with annual VLM rates exceeding 1 mm per year. In comparison, coastal regions in the United Kingdom, Ireland, and western France exhibit relatively moderate subsidence, with annual rates typically below 1 mm per year. In most areas of the Mediterranean coast of southern Europe, where the VLM is below 1 mm per year, the coastal zone is sinking more severely than in the countries north of the Mediterranean. When viewed from a finer spatial scale, coastal-to-inland VLM patterns show distinct regional contrasts (Fig. 2b). Subsidence-dominated coasts, such as the Atlantic–North Sea and Mediterranean–Black Sea regions,

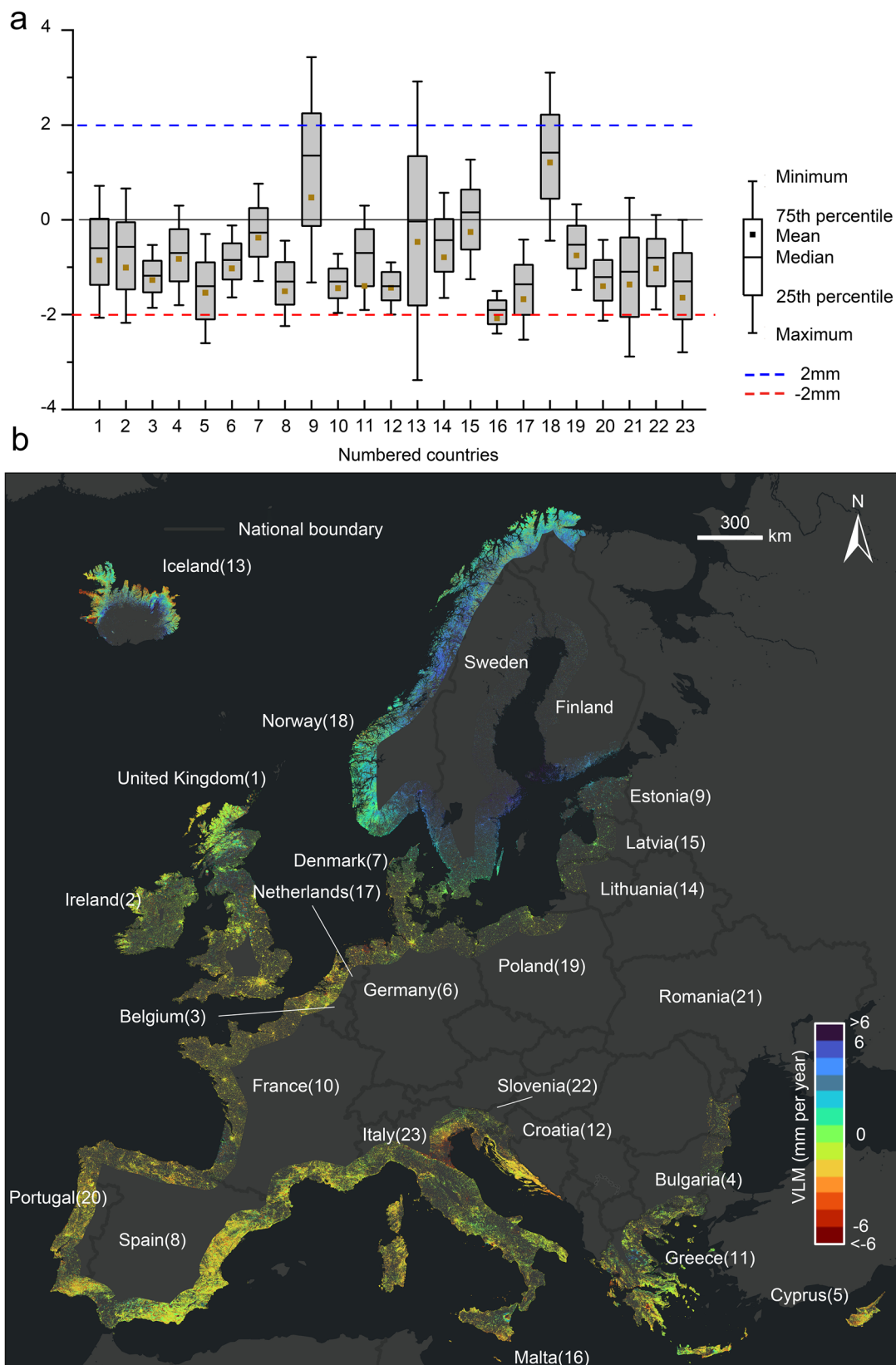


Fig. 1 | Vertical land motion data along the European coastal zone. a Box plot representing the distribution of VLM for 23 European countries in this study. The countries include: 1. United Kingdom; 2. Ireland; 3. Belgium; 4. Bulgaria; 5. Cyprus; 6. Germany; 7. Denmark; 8. Spain; 9. Estonia; 10. France; 11. Greece; 12. Croatia; 13. Iceland; 14. Lithuania; 15. Latvia; 16. Malta; 17. Netherlands; 18. Norway; 19. Poland; 20. Portugal; 21. Romania; 22. Slovenia; 23. Italy. **b** Spatial distribution of VLM along

the European coastal zone, based on data collected from 2019 to 2023. The 2019–2023 VLM patterns are reproducible across epochs, supporting the use of the 2019–2023 baseline for downstream land-cover and socioeconomic analyses. The map was created using ArcGIS Pro (version 3.1.5) with the light gray canvas base as the basemap. All elements in this figure were created by the authors.

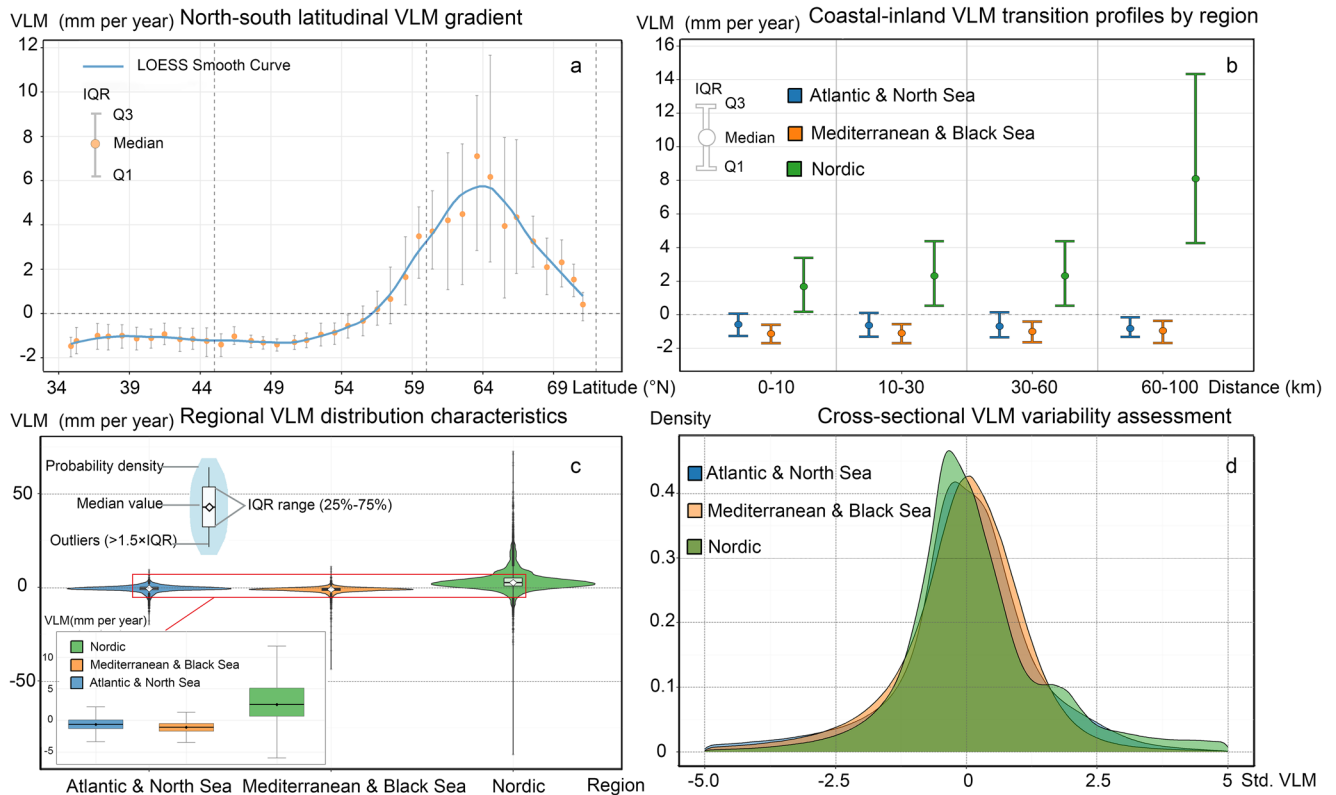


Fig. 2 | Spatial gradients and transition patterns of VLM across European coastal zones. **a** Latitudinal variations of VLM, showing the transition from Nordic uplift to Mediterranean subsidence. Orange dots are medians, and the blue line is a smooth curve. **b** Coastal-to-inland VLM transitions, grouped by distance. **c** VLM distribution across regions, compared with violin and box plots. **d** Standardized

VLM density distributions for each region, normalized using the median-MAD method. By synthesizing the latitudinal gradient at the continental scale, the coast-to-inland transition, and regional variability, this visualization provides the physical and statistical basis for the exposure framework.

display relatively uniform rates inland, whereas uplift-dominated northern areas exhibit a clear inland-increasing trend, highlighting Europe’s complex VLM dynamics.

Furthermore, Malta’s subsidence phenomenon warrants special attention, as localized VLM rates exceed 2 mm per year—well higher than the average for other Mediterranean coastal countries. With a limited land area of just 316 km², Malta’s geological structure is primarily composed of limestone, making it highly susceptible to karstification, which exacerbates subsidence-related risks and further constrains the country’s ability to adapt to environmental changes⁶¹. It can be seen that the surface material composition of different land cover influences their ability to enhance or mitigate the VLM. Europe, characterized by its highly indented coastline, hosts a large number of small islands. Owing to their limited resources, these islands inherently face major constraints, which exacerbate their vulnerability to climate change by restricting their adaptive capacity, making subsidence a critical risk factor that directly threatens their long-term sustainability^{62,63}. At the same time, the surface material composition of the coastal zone region is complex and diverse, and different VLM patterns influence the subsidence sensitivity pattern of different sites through the interplay of their rate variations, spatial heterogeneity, and physical attributes of the site types; thus, identifying the coupling relationship between VLM patterns and surface cover characteristics is crucial for disaster risk assessment in the European coastal zone.

Subsidence exposure of national land cover in coastal zones

Leveraging the 100 m resolution Urban Atlas 2018 dataset (100 m spatial resolution, 43 land use categories) from the Copernicus Earth Observation programme, this study assesses the spatial exposure patterns of four land systems along European coastal zones. Focusing on predominant coastal

Table 2 | Statistical of subsidence in the European coastal zone ground cover system

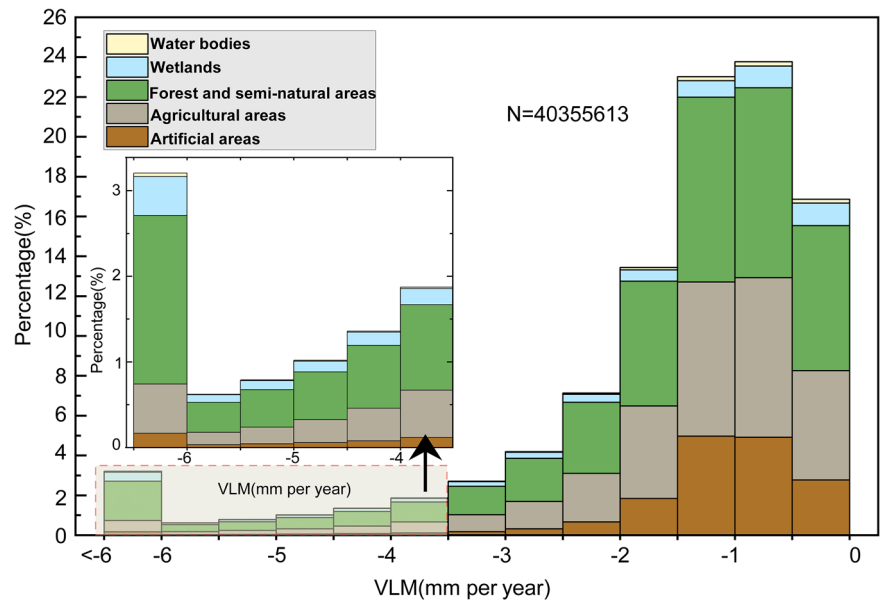
Urban Atlas 2018	% Subsidence	Subsidence (mm per year)
Artificial areas	16.2%	1.2 ± 1.6
Agricultural areas	32.7%	1.5 ± 1.9
Forest and semi-natural areas	44.6%	1.9 ± 3.1
Wetlands	5.6%	2.3 ± 3.1

% Subsidence represents the percentage of each site type in the subsidence area.

land cover types, artificial areas, agricultural areas, forested and semi-natural areas, and wetlands were selected as primary research targets. Analytical results demonstrate distinct spatial predominance: artificial areas, agricultural areas, forested/semi-natural areas, and wetlands account for 2.3%, 33.5%, 29.3%, and 2.0% of coastal land coverage, respectively. Interpolating the VLM values to the land use dataset, a comparative analysis of VLM rates revealed annual subsidence ranging from 1.2 to 2.3 mm per year across land cover types, with wetlands exhibiting notably higher mean subsidence rates of 2.3 ± 3.1 mm per year (Table 2).

Figure 3 reveals the spatial differentiation characteristics of land cover types under varying subsidence gradients along the European coastal zones. Throughout the total subsidence observation period (2019–2023), forested and semi-natural areas, along with agricultural areas, were the dominant land cover types in the primary subsidence regions of the European coastal zone, collectively accounting for nearly 80% of the affected areas. Artificial areas display concentrated subsidence values within the 0 to –4 mm per year range (peaking near –1 mm per year), with overall subsidence

Fig. 3 | Subsidence frequency distribution by land use covers. *N* is the number of pixels, and VLM is vertical land motion. The chart was created using Origin 2024. All elements in this figure were created by the authors.



magnitudes being relatively low. Whereas wetlands have the smallest total area among all land cover types, their subsidence levels in the European coastal zone are relatively high, with their share in subsidence-prone areas exceeding twice their total area percentage.

The spatial heterogeneity of subsidence may stem from climate change and the structural differences among land systems. Climate change increases the risk of intrusion of seawater and salinization, which exacerbate aquifer compression caused by groundwater extraction, leading to subsidence in forested and semi-natural areas^{64–66}. In highly irrigated agricultural lands, particularly in Mediterranean countries, such as Spain and Italy, subsidence is primarily driven by irrigation-induced shallow aquifer compression and the densification of the till layer due to mechanical compaction from agricultural machinery^{67–71}. Meanwhile, human activities, such as large-scale filling/emptying cycles of large underground water reservoirs, and underground space development (e.g., tunneling), inevitably contribute to a certain degree of subsidence in these man-made areas⁷². For wetlands, sediment compaction driven by tidal pumping effects and organic layer volume loss caused by aerobic decomposition of organic matter jointly accelerate subsidence, exacerbating the vulnerability of wetland ecosystems to relative SLR⁷³.

These variations in subsidence mechanisms among different land cover types directly shape their exposure to ground deformation and structural resilience. Artificial areas with high-density infrastructure and concentrated populations are particularly susceptible to secondary hazards, such as building fissures or pipeline damage, under pronounced subsidence. In contrast, less developed regions, including natural wetlands or agricultural lands, generally face lower exposure. Moreover, the functional criticality of specific land cover types means that even comparable settlement magnitudes can translate into different levels of economic and social risk. Collectively, the differential sensitivity of land cover types to subsidence generates pronounced spatial heterogeneity in exposure and potential impact.

The impact of relative sea level rise on coastal zones

Under the synergistic effects of global climate change and human activities, coastal inundation and erosion risks are exhibiting a pronounced intensification trend, with low-lying ecosystems and infrastructure facing multidimensional threats. The study focuses on the European coastal zone, integrating VLM and DEM datasets, combined with SSP2 4.5 SLR projections, to construct inundation risk maps under relative SLR scenarios. Potential inundation risk areas are systematically

quantified, with particular emphasis on revealing the inundation extent, affected population size, building density, and asset value under exposure scenarios. Furthermore, the spatial distribution characteristics of typical land cover types within identified risk-exposed areas are investigated to establish multidimensional references for coastal resilience planning.

The risk assessment results indicate that, under a scenario without any flood prevention measures, relative SLR is projected to expose approximately 94,000 km² of coastal land in Europe to inundation risks by 2050. Within these exposed areas, nearly 25 million residents and more than 8 million buildings are expected to be directly affected, accounting for 86% of the total coastal population and 6.8% of the total building stock in Europe, respectively. National-scale coastal exposure assessments (Fig. 4) reveal that Germany, the United Kingdom, and the Netherlands rank highest in terms of exposed land area, with respective exposure extents reaching 12,600, 12,300, and 9300 km², followed by France and Italy, each with exposure areas exceeding 8000 km². Regarding population exposure, the Netherlands, the United Kingdom, and Italy demonstrate the most severe impacts, with exposed populations reaching 4.7 million, 2.8 million, and 2.1 million, respectively, all surpassing the 3-million threshold. Of particular note is the Netherlands, where the number of exposed buildings reaches 3.5 million, with estimated asset values exceeding €3.4 trillion, far surpassing other European countries in both metrics.

Spatial analysis of land use composition within inundation risk exposure areas reveals distinctive distribution patterns, with artificial areas, agricultural areas, forest/semi-natural areas, and wetlands accounting for 10.9%, 67.1%, 7.9%, and 8.6% respectively. Agricultural areas emerge as the predominant exposed category, primarily distributed in low-lying zones and areas susceptible to hydrological alterations, rendering them particularly vulnerable to relative SLR impacts. This spatial configuration underscores the necessity for prioritizing risk mitigation strategies in agricultural zones. To further explore how exposure patterns are associated with artificial areas, we selected representative cases with typical population and infrastructure exposure across Europe. Analyses of the Netherlands, the United Kingdom, and Italy reveal strong correlations between subsidence patterns and the distribution of artificial areas. As illustrated in Fig. 5, the Netherlands exhibits pronounced subsidence concentrated in agricultural and artificial areas, particularly within major urban centers, including Amsterdam and the Hague. These subsidence hotspots demonstrate strong spatial correspondence with artificial area distribution. Similar spatial patterns are

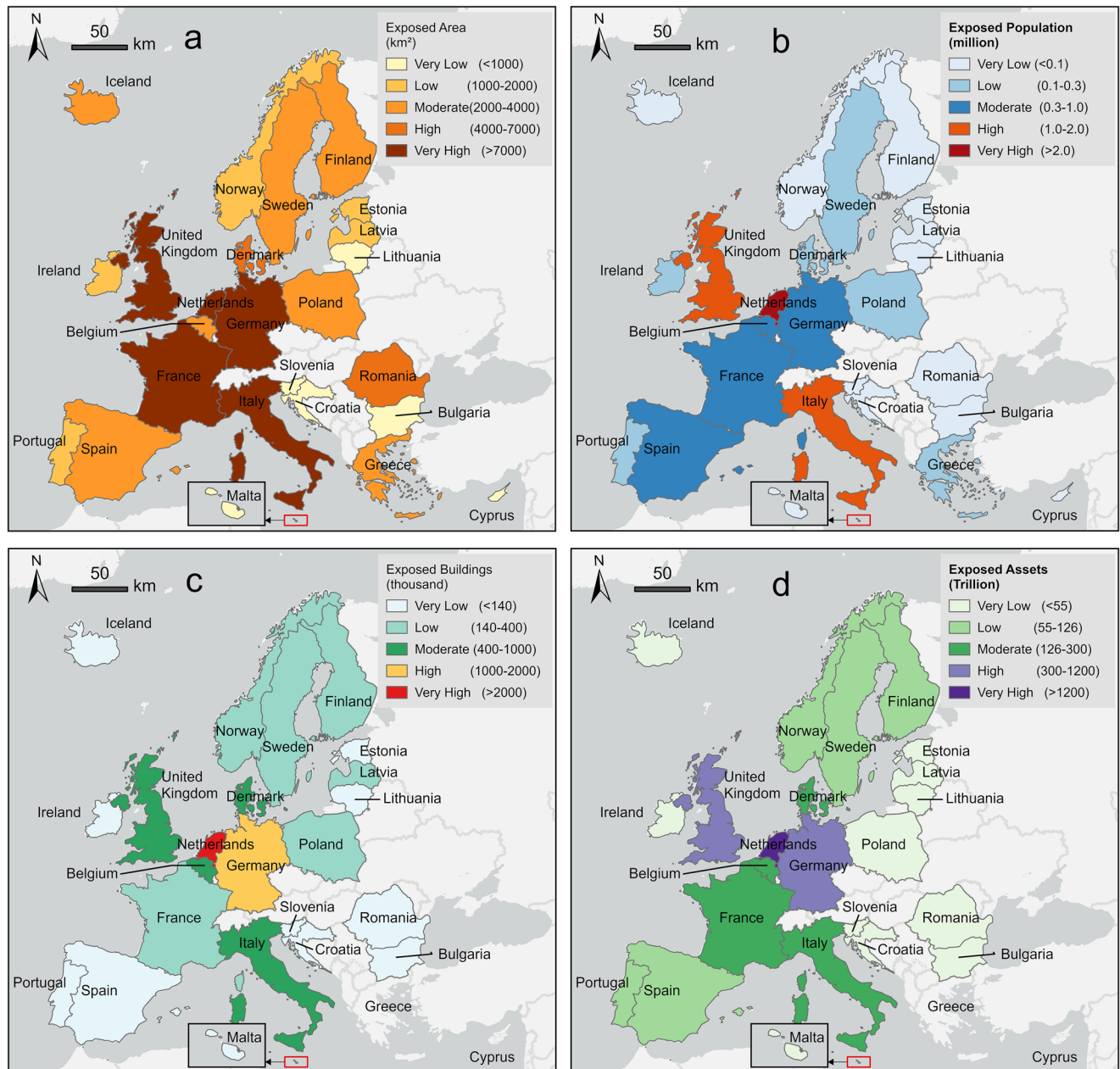


Fig. 4 | Exposure assessment of European coastal zones by 2050. The exposure assessment in this study is confined to coastal inundation zones, while a national-scale base map is displayed for cartographic clarity. **a** Distribution of exposed areas in European coastal countries. **b** Distribution of exposed population in European coastal countries. **c** Distribution of exposed buildings in European coastal countries. **d** Distribution of exposed assets in European coastal countries. The map was created using ArcGIS Pro (version 3.1.5) with the light gray canvas base as the basemap. All elements in this figure were created by the authors.

observed in the United Kingdom and Italy, where subsidence intensity shows positive correlation with artificial areas density, particularly in urbanized coastal areas.

The exposure risks along European coastlines stem from the interplay between natural geographical conditions and anthropogenic activities, exhibiting pronounced spatial heterogeneity in dominant drivers. The synergy between intense urbanization and land subsidence markedly amplifies inundation risks in artificial areas—exemplified by the Netherlands, where artificial areas constitute 56% of national exposure areas, predominantly concentrated in low-lying urban agglomerations such as Amsterdam and Rotterdam. The coupling of geomorphological features and subsidence effects shapes differentiated risk patterns: Italy emerges as a high-risk hotspot in the Mediterranean due to the interaction of lagoon-estuary complexes and regional land

subsidence. Of particular importance is the severe risk of inundation faced by agricultural areas along the European coast, and climate change will exacerbate many economic and social challenges already faced by these areas⁷¹. Given the dual importance of agricultural systems in ensuring food security and maintaining ecological functions, their high exposure underscores the necessity of prioritizing them in coastal risk management strategies⁷⁴. In addition to the combination of natural and anthropogenic factors, coastal risk is deeply embedded in the social fabric. Social vulnerability exhibits marked stratification and spatial differentiation, and this structural vulnerability leads to clear differences in the extent of damage and the speed of recovery from actual hazards among different regions and groups, even in similar geographically exposed environments, thus exacerbating differential vulnerability to coastal zone inundation risk.

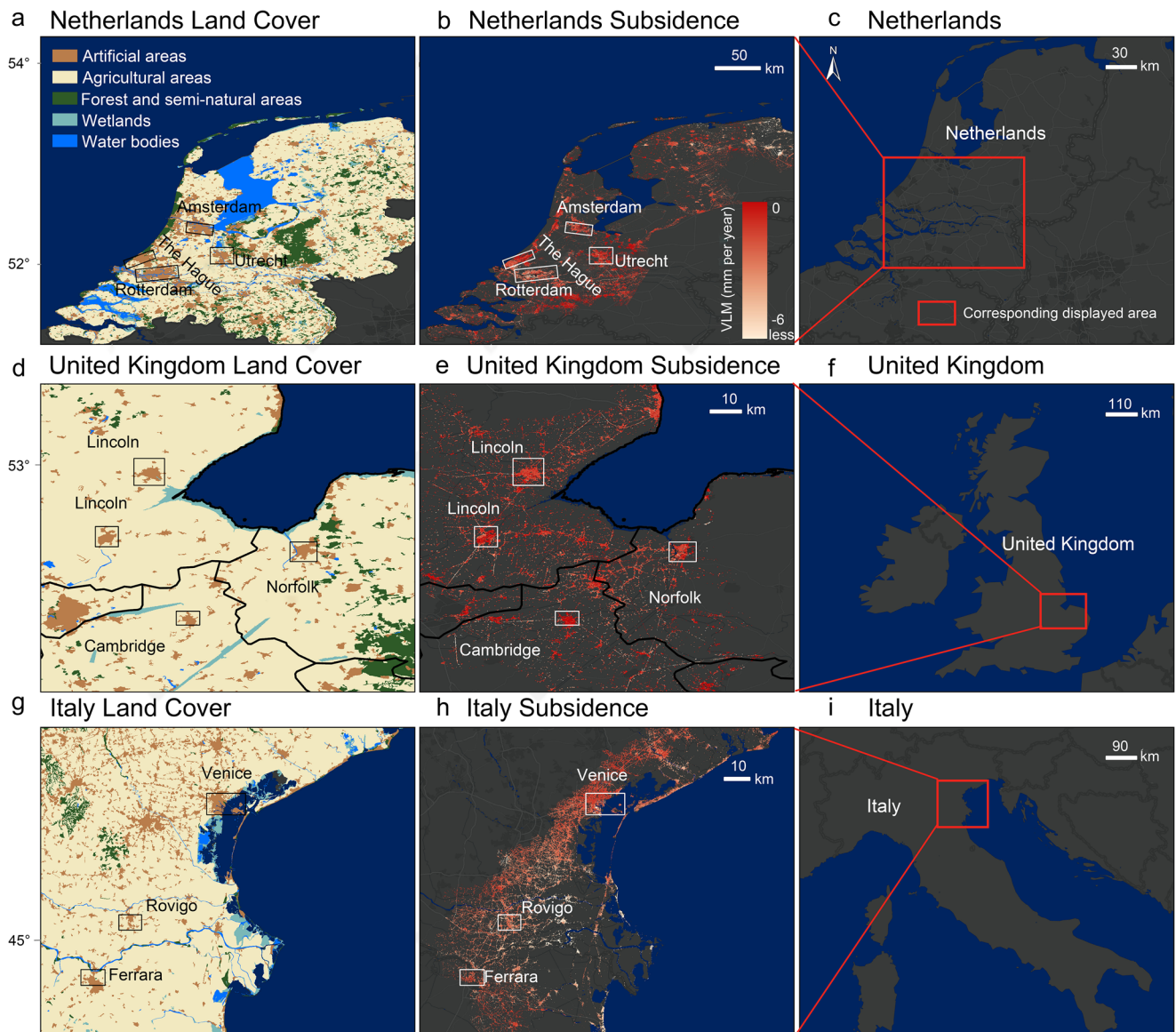


Fig. 5 | Examples of regions with high exposure to land subsidence. **a** National land cover map for the Netherlands area. **b** Land subsidence across the Netherlands. **c** Overview map that helps locate the relevant area within the Netherlands. **d** Land cover in parts of the United Kingdom. **e** Distribution of land subsidence in parts of the United Kingdom. **f** Overview map that helps locate the relevant area within the

United Kingdom. **g** Land cover in parts of Italy. **h** Distribution of land subsidence in parts of Italy. **i** Overview map that helps locate the relevant area within Italy. The map was created using ArcGIS Pro (version 3.1.5) with the light gray canvas base as the basemap. All elements in this figure were created by the authors.

Climate change inequality in coastal zones

Climate change imposes unequal and uneven burdens across regions, necessitating a more nuanced understanding of this global crisis⁷⁵. Climate risks are deeply coupled with social vulnerability, which is commonly assessed through indicators such as economic deprivation, dependent age structures, and systemic marginalization based on ethnic or group identity⁷⁶. These dimensions collectively characterize differences in sensitivity and adaptive capacity among social groups when facing environmental hazards. Within this context, the present study situates its assessment under the European Union’s Just Resilience objective, emphasizing that climate adaptation planning should ensure the inclusion and protection of the most vulnerable populations, including those differentiated by age, health status, economic conditions, and place of residence⁷⁷. Integrating this policy framework with the social structure of Europe, the situation of Roma communities provides a critical analytical focus: they are not only economically disadvantaged but also experience persistent social exclusion based on ethnic identity, rendering them particularly susceptible to compounded

inequalities under climate impacts^{78,79}. Accordingly, this study integrates economic, age, and ethnic dimensions to systematically assess the spatial distribution of climate risk along European coasts, thereby revealing patterns of social inequity that may persist despite the EU’s just resilience objectives.

To systematically analyze the impact of economic background on the differences in climate risk exposure across coastal areas, the exposed coastal geographical units of Europe (the smallest statistical district units for which data are available) are divided into four economic level stages based on the economic statistics of each country (Fig. 6). The proportions of geographical units within each stage from low to high are 25%, 24%, 22%, and 29%, respectively. Regional economic conditions are a critical factor in determining adaptive capacity, as higher economic-level cities typically possess more sufficient resources to implement systematic climate adaptation measures⁸⁰. Consequently, despite this overall balanced economic distribution across European coasts threatened by SLR, a marked adaptive capacity gap exists between economically developed

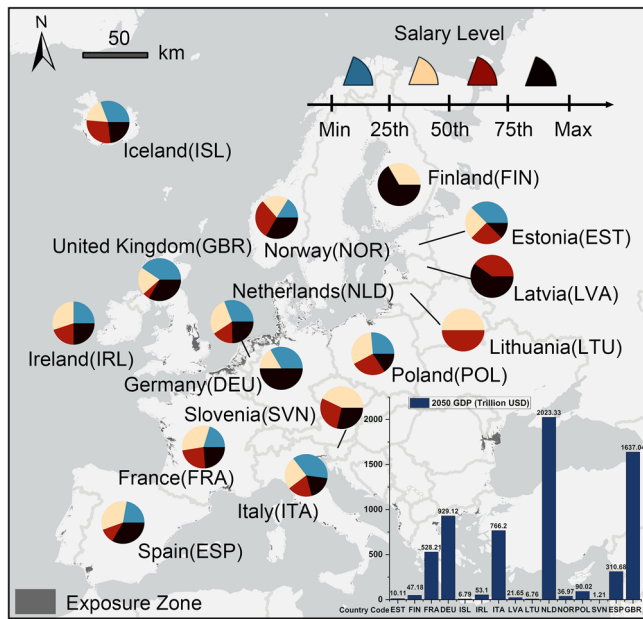


Fig. 6 | Distribution of salary levels by exposure zone in Europe. The pie chart shows the wage distribution of the exposed regions in the country, divided into four categories from low to high. The black shaded area is the submerged exposed area. The lower-right panel presents a bar chart of projected gross domestic product (GDP, in trillions of U.S. dollars) for selected European countries in 2050, providing a standardized reference for comparing the absolute economic capacity of the exposed countries⁹⁴. The map was created using ArcGIS Pro (version 3.1.5) with the light gray canvas base as the basemap. All elements in this figure were created by the authors.

cities, which can build resilient defense systems, and areas at a basic economic level.

While economic conditions set the baseline capacity for adaptation, demographic factors such as the proportion of older adults and children influence the degree of vulnerability within local populations. Analysis of the European coastal population exposure reveals the particular vulnerability of specific demographic groups. Older adults and children, whose capacity to cope with climate risks is often limited, currently constitute about 40% of the exposed population on average. Projections indicate this share will rise to 60% by 2050. Notable spatial disparities exist, from a high of 70% in Almería, Spain, to a still-substantial 58% in Kymenlaakso, Finland. This trend underscores increasing demographic vulnerability due to population aging, which will likely compound the challenges of future climate adaptation and risk mitigation strategies. Beyond age-related vulnerability, social and ethnic inequalities intersect with demographic factors, further shaping the exposure and adaptive capacity of marginalized groups.

Climate change exacerbates the vulnerability of marginalized groups through intersecting social inequalities⁸¹. The situation of the Roma, Europe’s largest ethnic minority, is a case in point. Data from the European Union Agency for Fundamental Rights (2021) show that, on average, 80% of the Roma population in 10 European countries lived at risk of poverty (with disposable income below 60% of the national median). Spain recorded the highest rate, at 98%, indicating severe economic marginalization⁷⁹.

In Spain, the Roma population is concentrated primarily in the southeastern regions. Key coastal cities within these regions, such as Seville and Valencia, face high flood exposure risks. These cities also rank among the highest in Spain in terms of the number of Roma communities, settlements, and housing units, creating a spatial overlap that compounds exposure and vulnerability. Furthermore, poor housing conditions prevalent among low-income Roma communities, which often lack structural resilience, increase their susceptibility to natural disasters and extreme weather events⁸².

Disparities in insurance coverage further reveal institutional gaps. As noted by the World Health Organization, traditional community-based health insurance schemes have had limited success in providing universal coverage, and poor and marginalized groups rarely receive adequate support⁸³. This lack of access to formal financial protection limits the post-disaster recovery capacity of socioeconomically disadvantaged groups. Thus, land subsidence, poor housing conditions, and the unevenness of institutional support collectively amplify the overall risk faced by Roma communities in high-risk coastal areas.

In summary, pronounced disparities in exposure, vulnerability, and adaptive capacity exist across different groups and regions under climate change. Although socially marginalized populations and low-income areas may constitute a small fraction of the coastal zone spatially, the impacts they suffer can be profound and long-lasting. Pre-existing inequalities are amplified by climate impacts, deepening the vulnerability of disadvantaged groups and creating a vicious cycle of escalating risk that raises serious social justice concerns¹⁴.

A deeper look at VLM patterns, land cover, coastal exposure patterns, and social structure heterogeneity reveals that natural physical processes are not spatially isolated, but rather intertwined with social vulnerability. High subsidence areas tend to coincide with low-lying, highly urbanized areas, and these areas with high concentrations of population and infrastructure are prone to higher exposure risks in the context of relative SLR. Meanwhile, in these high-risk areas, groups with weaker socio-economic conditions and poorer adaptive capacity are more vulnerable to shocks in the face of environmental changes and extreme events, thus forming a risk aggregation area characterized by high subsidence, high exposure, and high vulnerability. It can be seen that the spatial aggregation of risk is not accidental, but is the result of long-term interaction between natural processes and social structures. The complex dynamics of risk highlight the multidimensional nature of potential risks in coastal areas, offering a broader perspective for future research.

Conclusions

This study presents a unified and systematic assessment of subsidence in European coastal nations. Along the Atlantic coast of western Europe, subsidence remains relatively moderate, with annual subsidence rates generally below 2 mm per year. In contrast, the Mediterranean coast of southern Europe exhibits a stronger subsidence trend, particularly in small island nations, where resource constraints and high-intensity human activities exacerbate the issue. Agriculture and forests, as the dominant land cover types in the European coastal zone, are prevalent in subsidence areas. However, the proportion of artificial surfaces in subsidence areas is considerably higher than their overall share of land cover. Notably, subsidence hotspots in high inundation risk countries, such as the Netherlands and the United Kingdom, exhibit pronounced overlap with artificial areas, underscoring the role of human activities in driving disaster exposure. As critical ecosystems, wetlands account for only 2% of the coastal zone yet exhibit the highest subsidence rates, and thus the unique geohydrological characteristics of wetlands should be fully considered in coastal adaptation planning.

Under climate change, the combined effects of land subsidence and SLR pose substantial risks and economic losses to Europe’s coastal zones. The adaptive capacity of different regions follows a pronounced socioeconomic gradient, where economically developed areas generally demonstrate stronger climate resilience, whereas less developed regions face systemic resilience deficits. Among the exposed areas in the study region, the number of low-development zones is nearly equivalent to that of highly developed cities, presenting a dual challenge for coastal risk management—both safeguarding critical infrastructure and economic assets in high-development cities and enhancing the adaptive capacity of less developed regions. Additionally, older adults (>65 years) and children (<15 years) constitute 40% of the exposed population, with their limited mobility and adaptive resources exacerbating their vulnerability. Moreover, the overconcentration of marginalized

communities, such as the Roma population, within high-risk zones, combined with their limited policy engagement, creates a reinforcing cycle of vulnerability that requires intervention through inclusive governance strategies.

Understanding land subsidence and its driving factors in the European coastal zone is essential for assessing and mitigating coastal inundation risk. Despite certain limitations in spatial resolution and temporal frequency, the EGMS still provides a valuable source of surface deformation data across Europe, laying a scientific foundation for transboundary geohazard prevention and climate change response, while demonstrating strong potential for supporting cross-regional comparisons and long-term trend assessments. The main contribution of this study lies in building on a validated VLM mapping framework and integrating it with land cover and socio-economic indicators to construct a multi-source exposure risk framework, offering an integrated perspective for investigating subsidence-related hazards and social inequalities.

Nevertheless, several limitations should be acknowledged. First, the bathtub method itself has inherent constraints. Based on a static assumption of free water filling, it does not account for tidal dynamics, hydrodynamic processes, or drainage systems, which may affect the accuracy of the predictions. Second, in measuring asset exposure, we focus on building values to capture the potential direct losses to private wealth. This provides an important complement to existing GDP-based analyses; however, a comprehensive economic risk assessment should also incorporate public, commercial, and industrial assets. Third, in the treatment of economic indicators, converting values into within-country percentiles preserves the national context but obscures absolute cross-country differences, thereby limiting interpretations of adaptive capacity across nations. Finally, in terms of demographic structure, this study adopts future age-composition scenarios to better reflect projected population changes, yet the assumption that subnational trends follow national-level dynamics may not fully capture local heterogeneity.

Future research could build on this foundation by incorporating dynamic hydrological processes to more realistically simulate inundation patterns, while integrating multi-dimensional asset data, higher-resolution demographic information, and more detailed land-use classifications. Such refinements would enable a more nuanced identification of vulnerabilities across different built environments, contributing to a more comprehensive understanding of coastal subsidence risk and its inequalities. These efforts would also provide stronger scientific support for enhancing climate resilience and long-term spatial planning in European coastal regions.

Methods

Vertical land motion data

This study leverages interferometric synthetic aperture radar data from the Sentinel-1 satellite, provided by the EGMS. The analysis specifically utilizes the EGMS-derived ortho product, referenced to a geocentric coordinate framework⁵⁰. With a spatial resolution of approximately 100 meters, this dataset enables high-precision detection and quantification of ground motion across Europe at the millimeter scale. The 2019–2023 EGMS Ortho vertical velocity field serves as our baseline for all main-text spatial summaries and socioeconomic integration. The 2018–2022 epoch is used only for an inter-epoch consistency check.

The VLM data use the European Terrestrial Reference System 1989—Lambert azimuthal equal-area projection coordinate system, which facilitates spatial analysis on a European scale. This coordinate system was chosen for its ability to minimize distortion in area representation, making it particularly suitable for continental-scale studies. For this study, subsiding land was defined as all areas exhibiting a VLM rate of less than 0 mm per year. Based on the availability of consistent and high-quality data, annual mean VLM data for the periods 2018–2022 and 2019–2023 were acquired to characterize the trends of land movement in the inland regions of the European coastal zone, enabling a robust comparison of temporal changes in ground motion. By comparing the velocity changes between the two

periods, the study aimed to reveal the acceleration or deceleration characteristics of land subsidence or uplift, thereby quantifying the dynamic changes in VLM rates across coastal areas. Subsequently, the VLM data were integrated to perform a detailed analysis of the subsidence characteristics in various regions of the European coastal zone, aiming to uncover the spatial distribution and regional variability of subsidence changes (Fig. 1).

In this study, the European coastal zone is defined as the area extending up to 100 kilometers inland from the coastline of European seas. This distance is consistent with previous large-scale coastal studies, as it captures the socio-economic and environmental characteristics of coastal regions while ensuring analytical feasibility at the continental scale^{14,51,84}. To delineate this zone, the `ne_10m_coastline` dataset (<https://www.naturalearthdata.com/downloads/10m-physical-vectors/10m-coastline/>) from Natural Earth was used as the base, clipped to the European region. A 100-kilometer inland buffer was then generated to represent the coastal zone for spatial analysis. VLM data within this delineated study area were systematically extracted, and areas with sparse or discontinuous data points were excluded to ensure data reliability. The analysis encompassed 25 countries within the European coastal zone, namely Belgium, Bulgaria, Croatia, Cyprus, Denmark, Estonia, Finland, France, Germany, Greece, Iceland, Ireland, Italy, Latvia, Lithuania, Malta, Netherlands, Norway, Poland, Portugal, Romania, Slovenia, Spain, Sweden, and the United Kingdom. This selection was based on the geographical distribution of coastal regions and the availability of high-quality InSAR data, ensuring a representative sample of European coastal dynamics and facilitating a comprehensive assessment of VLM trends and their spatial variability across the European coastal regions.

National land cover data

This study utilized the 2018 European land cover map (Urban Atlas 2018), released by the Copernicus Earth observation programme, which provides detailed spatial information on land surface characteristics across Europe. The Urban Atlas 2018 encompasses 43 land cover categories and was employed in this research as a grid map with a spatial resolution of 100 meters. For the purposes of this study, four primary land cover types were selected: artificial areas (land cover types where the original natural environment has been fundamentally altered by human activity), agricultural areas, forests and semi-natural areas, and wetlands. These categories were chosen to represent the dominant land cover types in coastal regions and to assess their varying responses to environmental changes such as land subsidence and inundation risks.

To evaluate the subsidence exposure of various coastal systems along Europe's coastline, VLM values were interpolated onto a land cover map. This process ensured that the VLM values were accurately represented across different land cover types, allowing for the extraction of corresponding VLM values for each land cover pixel. In order to quantify the distribution characteristics of different land cover types within the VLM range of 0 to -6 mm per year, this study calculated the pixel proportion of each land cover type in this interval (Fig. 3)⁵¹. This approach provided a detailed understanding of how land subsidence varies across different land cover types, particularly in areas experiencing moderate to high subsidence rates.

Based on the spatial distribution data of land subsidence, this study employed pixel-based statistical methods to calculate the proportion of subsidence pixels within each land cover type. This approach enabled a quantitative assessment of the differential impacts of land subsidence on various land cover types, highlighting the varying susceptibility of artificial areas, agricultural areas, forests and semi-natural areas, and wetlands to subsidence. Furthermore, to explore the relationship between land cover and inundation risks, the spatial distribution information of land cover within inundation risk zones was extracted (See Supplementary Fig. 2). By analyzing the spatial pattern characteristics of land cover within these zones, the study identified the distribution patterns of land cover types associated with potential inundation risks.

Exposure assessment

We used a bathtub model to predict flood risk in European coastal countries (See Supplementary Fig. 3)^{14,85–87}. The evaluation mainly used the following datasets:

VLM (vertical land motion): ground motion data for the European coastal zone at a standard resolution (100 m), sourced from the EGMS.

DEM (digital elevation model): a 30 m resolution DEM from the Copernicus Programme, serving as the baseline topographic dataset.

SLR (sea level rise): projected geocentric SLR estimates under the SSP2-4.5 scenario, derived from IPCC assessment reports.

MSL (mean sea level): standardized MSL referenced to a global datum (See Supplementary Fig. 4), provided by the permanent service for mean sea level (<https://psmsl.org/data/obtaining/complete.php>)⁸⁸.

The VLM rates are resampled to match the 30 m resolution of the DEM using bilinear interpolation. Assuming the 2019–2023 VLM rate persists from 2022 to 2050 (constant-rate baseline), the elevation is projected from the DEM reference year (2022) to the target year (2050)¹⁴.

$$DEM_{mod} = DEM_{2022} + VLM \times \Delta t \quad (1)$$

In which DEM_{mod} represents the projected future elevations (2050) after adjusting for VLM; DEM_{2022} provides the initial elevation data for 2022; VLM is used to quantify the annual uplift or subsidence of the land surface; Δt is a time-dependent adjustment factor (in years), converting the VLM rate to cumulative elevation change over the period from 2022 to the target year (2050, $\Delta t = 28$). We carry forward the empirically observed 2019–2023 VLM rate to 2050 as a constant-rate baseline.

Meanwhile, based on the SSP2-4.5 scenario predicted by IPCC, the median SLR rate was selected to estimate the sea level by 2050. To avoid duplicate calculations of ground subsidence, the novlm (no VLM) version is used for prediction. During the prediction process, the SLR rate is assigned to the nearest tidal station, and the adjusted tidal station data is used to predict the 2050 sea level. Finally, the inundation risk is evaluated by subtracting the adjusted DEM elevation from the estimated average sea level (Eq. 2)¹⁴.

$$Inun = DEM_{mod} - (SLR_{50} + MSL) \quad (2)$$

In which $Inun$ represents the estimated exposure value; DEM_{mod} is the corrected elevation model updated using the VLM projections; SLR_{50} represents the 50th percentile of IPCC’s prediction of global SLR by 2050; and MSL denotes the mean sea level.

To delineate spatially continuous submerged units, a connectivity analysis is conducted on the computed results. Under the assumption that no flood control measures are implemented, regions exhibiting negative exposure values in the analysis are identified as high-risk coastal flood zones by 2050. Following the identification of these exposure zones, subsequent analyses quantify the vulnerability of three key coastal elements: (1) land area, (2) population, and (3) buildings. Population exposure was quantified by extracting and aggregating projected population data for the year 2050 under the SSP2 scenario within the delineated inundation zones (See Supplementary Table 2)⁸⁹. Building exposure assessment utilized Microsoft’s Building Footprints dataset to count the number of structures located in exposed areas⁹⁰. For economic impact analysis, country-level housing price data (See Supplementary Table 3) were integrated from Statista and Numbeo databases (<https://www.numbeo.com/cost-of-living/>)⁹¹. Assuming the affected properties are a total loss, the potential economic loss caused by relative SLR was estimated by calculating the product of the total exposed built-up area and the property price per unit area.

Socioeconomic and demographic data

To comprehensively investigate the different responses of European coastal countries to the pressing challenge of relative SLR, we systematically collected statistical data for the exposed areas, including economic and demographic indicators from the official statistical offices of various

European countries. The dataset consists of the most recently published annual or monthly data from each country’s national statistical office, with the geographic granularity determined by the smallest administrative unit level for which data is made publicly available in each respective country. The exposed population and assets were then aggregated to the national level to produce the final results for international comparison. This approach ensures that the country-scale estimates are grounded in detailed spatial calculations.

Given that the economic indicators provided by each country do not adhere to a uniform standard across Europe, we transformed the raw economic values of individual geographic units into their corresponding percentile rankings relative to the national distribution. This standardization facilitates more accurate and meaningful comparisons across different countries, while preserving the relative economic standing of each unit within its national context.

During the data standardization process, the study employs a quartile-based classification system to categorize economic indicators across all geographic units at the national level. Specifically, the economic data are stratified into four distinct percentile ranges: (1) lower quartile (below the 25th percentile), (2) lower-middle quartile (25th to 50th percentile), (3) upper-middle quartile (50th to 75th percentile), and (4) upper quartile (above the 75th percentile). This methodological framework enables the systematic analysis of economic data distribution patterns within inundation-prone geographic units. Through this approach, the analysis can effectively assess the relative economic development levels of vulnerable coastal regions within their national contexts, providing critical insights into their differential susceptibility and adaptive capacity in response to relative SLR.

Based on the most recent national census data, we systematically collected demographic information pertaining to population cohorts aged 65 and above and under 14 in the submerged risk area. To project future demographic changes, we calculated a national-level population change factor using age structure data (share of population aged 0–14 and 65+) for 2024 and 2050, sourced from the World Population Prospects 2024 published by the United Nations⁹².

$$f_{c,age} = \frac{q_{c,age}^{2050}}{q_{c,age}^{2024}} \quad (3)$$

Where $q_{c,age}^{2024}$ and $q_{c,age}^{2050}$ are the national population shares of age group age in country c for 2024 (WPP estimate) and 2050 (WPP projection), respectively. This factor $f_{c,age}$ projects the relative change in the national age structure.

$$\bar{r}_{A,age}^{2050} = r_{A,age}^{2024} \times f_{c,age} \quad (4)$$

This estimates the future absolute share $\bar{r}_{A,age}^{2050}$ of age group age in study area A for 2050, by applying the national change factor ($f_{c,age}$) to its initial local share ($r_{A,age}^{2024}$).

$$r_{A,age}^{2050} = \frac{\bar{r}_{A,age}^{2050}}{\sum_{age_k} \bar{r}_{A,age_k}^{2050}} \quad (5)$$

Here, age_k denotes all age groups within study area A (including the specific age group of interest). This final step normalizes the projected shares from Eq. (4) so that the proportions for all age groups within area A sum to 100%.

Regarding the Roma population, our study incorporates related reports from the European Union Agency for Fundamental Rights, focusing particularly on poverty indicators and socio-economic challenges⁷⁹. This data provides crucial insights into the broader social context of Roma communities across Europe. Furthermore, through community data from the Spanish Gypsy Foundation, we have been able to establish spatial distribution patterns of Roma settlements, enabling us to examine potential correlations between their residential locations and flood-prone areas (See Supplementary Table 4)⁹³.

Reporting summary

Further information on research design is available in the Nature Portfolio Reporting Summary linked to this article.

Data availability

The vertical land motion data used in this study are publicly available from <https://egms.land.copernicus.eu/>. Copernicus 30 m digital elevation model (DEM) data are publicly available from the Copernicus data space ecosystem (<https://dataspace.copernicus.eu/explore-data/data-collections/copernicus-contributing-missions/collections-description/COP-DEM>) and related portals. Land cover data can be accessed from the Copernicus Land Monitoring Service: <https://land.copernicus.eu/en/products/corine-land-cover>. Sea-level rise data are available from the World Data Center for Climate: <https://www.wdc-climate.de/ui/>. The supporting datasets (including land use, population, asset, demographic, and tidal observation data) generated during this study are publicly available via Figshare: <https://doi.org/10.6084/m9.figshare.30866342>. All other data generated or analyzed in this study are available through the sources listed above and in the references cited within the main text.

Code availability

The code used to download the European Ground Motion Service European vertical land motion data is publicly available and has been deposited in Figshare: <https://doi.org/10.6084/m9.figshare.30866342>.

Received: 28 June 2025; Accepted: 5 January 2026;

Published online: 14 January 2026

References

1. Neumann, B., Vafeidis, A. T., Zimmermann, J. & Nicholls, R. J. Future coastal population growth and exposure to sea-level rise and coastal flooding—a global assessment. *PLoS ONE* **10**, <https://doi.org/10.1371/journal.pone.0118571> (2015).
2. Small, C. & Nicholls, R. J. A global analysis of human settlement in coastal zones. *J. Coast. Res.* **19**, 584–599 (2003).
3. Xiang, Z. Y., Li, Y. F. & Zhang, Z. Global conservation priorities of coastal habitats towards extreme sea level rise risks. *J. Clean. Prod.* **473**, <https://doi.org/10.1016/j.jclepro.2024.143455> (2024).
4. Li, D. et al. Temporal-spatial change of China's coastal ecosystem resilience and driving factors analysis. *Ocean Coast. Manag.* **255**, <https://doi.org/10.1016/j.ocecoaman.2024.107209> (2024).
5. Millennium Ecosystem Assessment. In *Ecosystems and Human Well-being: Synthesis* (Island Press, 2005).
6. Costanza, R. et al. The value of the world's ecosystem services and natural capital (reprinted from Nature, vol 387, pg 253, 1997). *Ecol. Econ.* **25**, 3–15 (1998).
7. Ferro-Azcona, H. et al. Adaptive capacity and social-ecological resilience of coastal areas: a systematic review. *Ocean Coast. Manag.* **173**, 36–51 (2019).
8. Turner, R. K., Subak, S. & Adger, W. N. Pressures, trends, and impacts in coastal zones: interactions between socioeconomic and natural systems. *Environ. Manag.* **20**, 159–173 (1996).
9. He, Q. & Silliman, B. R. Climate change, human impacts, and coastal ecosystems in the Anthropocene. *Curr. Biol.* **29**, R1021–R1035 (2019).
10. Wu, G., Liu, Q., Xu, H. & Wang, J. Modelling the combined impact of sea level rise, land subsidence, and tropical cyclones in compound flooding of coastal cities. *Ocean Coast. Manag.* **252**, 107107 (2024).
11. Abdulla, C., Al-Kuwari, H. A.-S., Aboobacker, V., Sadooni, F. N. & Vethamony, P. Sea-level rise along the coast of Qatar, central Arabian gulf under ongoing global warming and climate change. *J. Coast. Res.* **113**, 195–199 (2025).
12. Teatini, P., Ferronato, M., Gambolati, G., Bertoni, W. & Gonella, M. A century of land subsidence in Ravenna, Italy. *Environ. Geol.* **47**, 831–846 (2005).
13. Wigley, T. M. L. & Raper, S. C. B. Implications for climate and sea-level of revised IPCC emissions scenarios. *Nature* **357**, 293–300 (1992).
14. Ohenhen, L. O., Shirzaei, M., Ojha, C., Sherpa, S. F. & Nicholls, R. J. Disappearing cities on US coasts. *Nature* **627**, <https://doi.org/10.1038/s41586-024-07038-3> (2024).
15. Tay, C. et al. Sea-level rise from land subsidence in major coastal cities. *Nat. Sustain.* **5**, 1049–1057 (2022).
16. Anzidei, M. et al. Multi-temporal relative sea level rise scenarios up to 2150 for the Venice Lagoon (Italy). *Remote Sens.* **17**, <https://doi.org/10.3390/rs17050820> (2025).
17. Yu, H. R., Gong, H. L. & Chen, B. B. Analysis of the superposition effect of land subsidence and sea-level rise in the Tianjin coastal area and its emerging risks. *Remote Sens.* **15**, <https://doi.org/10.3390/rs15133341> (2023).
18. Duffy, C. E., Braun, A. & Hochschild, V. Surface subsidence in urbanized coastal areas: PSI methods based on Sentinel-1 for Ho Chi Minh city. *Remote Sens.* **12**, <https://doi.org/10.3390/rs12244130> (2020).
19. Wu, P. C., Wei, M. & D'Hondt, S. Subsidence in coastal cities throughout the world observed by InSAR. *Geophys. Res. Lett.* **49**, <https://doi.org/10.1029/2022gl098477> (2022).
20. Jongman, B., Ward, P. J. & Aerts, J. Global exposure to river and coastal flooding: long term trends and changes. *Glob. Environ. Change Hum. Policy Dimens.* **22**, 823–835 (2012).
21. Hanson, S. et al. A global ranking of port cities with high exposure to climate extremes. *Clim. Change* **104**, 89–111 (2011).
22. Nicholls, R. J. et al. Ranking port cities with high exposure and vulnerability to climate extremes: interim analysis: exposure estimates (OECD Publishing, 2007).
23. Shirzaei, M. et al. Measuring, modelling and projecting coastal land subsidence. *Nat. Rev. Earth Environ.* **2**, 40–58 (2021).
24. Nicholls, R. J. et al. A global analysis of subsidence, relative sea-level change and coastal flood exposure. *Nat. Clim. Change* **11**, 338–U382 (2021).
25. Løvholt, F. et al. Tsunami hazard and exposure on the global scale. *Earth Sci. Rev.* **110**, 58–73 (2012).
26. Tonini, R. et al. Testing tsunami inundation maps for evacuation planning in Italy. *Front. Earth Science* **9**, <https://doi.org/10.3389/feart.2021.628061> (2021).
27. Jasechko, S., Perrone, D., Seybold, H., Fan, Y. & Kirchner, J. W. Groundwater level observations in 250,000 coastal US wells reveal scope of potential seawater intrusion. *Nat. Commun.* **11**, <https://doi.org/10.1038/s41467-020-17038-2> (2020).
28. Mastrocicco, M. & Colombani, N. The issue of groundwater salinization in coastal areas of the Mediterranean region: a review. *Water* **13**, <https://doi.org/10.3390/w13010090> (2021).
29. van Asselen, S. et al. The relative contribution of peat compaction and oxidation to subsidence in built-up areas in the Rhine-Meuse delta, the Netherlands. *Sci. Total Environ.* **636**, 177–191 (2018).
30. Turner, R. E. & Ohimain, E. I. Dredged canals, wetland loss, and legacy. *Estuaries Coasts* **47**, 2147–2159 (2024).
31. Li, G., Chen, Y., Zhang, M. & Gong, X. *IOP Conference Series: Earth and Environmental Science* (IOP Publishing, 2019).
32. Russel, D. et al. Policy coordination for national climate change adaptation in Europe: all process, but little power. *Sustainability* **12**, <https://doi.org/10.3390/su12135393> (2020).
33. Nahlik, A. M. & Fennessy, M. S. Carbon storage in US wetlands. *Nat. Commun.* **7**, <https://doi.org/10.1038/ncomms13835> (2016).
34. Cohen, K. M., Cartelle, V., Barnett, R., Busschers, F. S. & Barlow, N. L. M. Last interglacial sea-level data points from northwest Europe. *Earth Syst. Sci. Data* **14**, 2895–2937 (2022).
35. Carrillo, E. et al. Tectono-sedimentary evolution of transverse extensional faults in a foreland basin: response to changes in tectonic plate processes. *Basin Res.* **32**, 1388–1412 (2020).

36. Parks, M. M. et al. 2021–2023 unrest and geodetic observations at Askja volcano, Iceland. *Geophys. Res. Lett.* **51**, <https://doi.org/10.1029/2023gl106730> (2024).
37. Jungdal-Olesen, G., Pedersen, V. K., Andersen, J. L., Gomez, N. & Mitrovica, J. X. Sea level response to late Pliocene-quaternary erosion and deposition in Scandinavia. *Quat. Sci. Rev.* **301**, 107938 (2023).
38. Schettino, A. & Turco, E. Plate kinematics of the western Mediterranean region during the Oligocene and early Miocene. *Geophys. J. Int.* **166**, 1398–1423 (2006).
39. Pondrelli, S. et al. European-Mediterranean regional centroid-moment tensors: 1997–2000. *Phys. Earth Planet. Inter.* **130**, 71–101 (2002).
40. Foest, J. P. et al. Methana magmatic observational experiment (MeMaX)- seismological monitoring of magmatic and tectonic activity in the western Saronic Gulf region, Greece. *Ann. Geophys.* **68**, <https://doi.org/10.4401/ag-9155> (2025).
41. de Louw, P. G. B., Bootsma, H., Kooi, H., Kramer, M. & Erkens, G. Land subsidence by peat oxidation leads to enhanced salinization through boils in Dutch polders. *E3S Web Conf.* **54**, 00007 (2018).
42. Molinaroli, E., Guerzoni, S. & Suman, D. Do the adaptations of Venice and Miami to sea level rise offer lessons for other vulnerable coastal cities? *Environ. Manag.* **64**, 391–415 (2019).
43. Ninfo, A., Ciavola, P. & Billi, P. The Po delta is restarting progradation: geomorphological evolution based on a 47-years Earth observation dataset. *Sci. Rep.* **8**, <https://doi.org/10.1038/s41598-018-21928-3> (2018).
44. Fleuchaus, P. & Blum, P. Damage event analysis of vertical ground source heat pump systems in Germany. *Geotherm. Energy* **5**, <https://doi.org/10.1186/s40517-017-0067-y> (2017).
45. Tosi, L., Teatini, P. & Strozzi, T. Natural versus anthropogenic subsidence of Venice. *Sci. Rep.* **3**, <https://doi.org/10.1038/srep02710> (2013).
46. Carbognin, L., Teatini, P. & Tosi, L. Eustacy and land subsidence in the Venice Lagoon at the beginning of the new millennium. *J. Mar. Syst.* **51**, 345–353 (2004).
47. Gatto, P. & Carbognin, L. T. H. E. Lagoon of Venice-natural environmental trend and man-induced modification. *Hydrol. Sci. Bull. Bull. Des. Sci. Hydrol.* **26**, 379–391 (1981).
48. European Commission. Communication on The European Green Deal. Communication from the Commission, COM(2021) 801 final, 2021/0421(NLE), Strasbourg, 14 December 2021. Available at: <https://eur-lex.europa.eu/legal-content/EN/TXT/?uri=CELEX:52021DC0801>.
49. Council of the European Union. Council Recommendation on ensuring a fair transition towards climate neutrality. 2022/C 243/04, 16 June 2022. Available at: https://eur-lex.europa.eu/legal-content/EN/TXT/?uri=OJ:JOC_2022_243_R_0004.
50. Thiéblemont, R. et al. Assessing current coastal subsidence at continental scale: insights from Europe using the European ground motion service. *Earth's Future* **12**, <https://doi.org/10.1029/2024ef004523> (2024).
51. Ohenhen, L. O., Shirzaei, M., Ojha, C. & Kirwan, M. L. Hidden vulnerability of US Atlantic coast to sea-level rise due to vertical land motion. *Nat. Commun.* **14**, <https://doi.org/10.1038/s41467-023-37853-7> (2023).
52. Peltier, W. R., Argus, D. F. & Drummond, R. Space geodesy constrains ice age terminal deglaciation: the global ICE-6G_C (VM5a) model. *J. Geophys. Res. Solid Earth* **120**, 450–487 (2015).
53. Faccenna, C. et al. Mantle dynamics in the Mediterranean. *Rev. Geophys.* **52**, 283–332 (2014).
54. Nordman, M., Poutanen, M., Kairus, A. & Virtanen, J. Using the Nordic geodetic observing system for land uplift studies. *Solid Earth* **5**, 673–681 (2014).
55. Joud, M. S. S., Sjöberg, L. E. & Bagherbandi, M. Use of GRACE data to detect the present land uplift rate in Fennoscandia. *Geophys. J. Int.* **209**, 909–922 (2017).
56. Simpson, M. J. R. et al. Projected 21st century sea-level changes, observed sea level extremes, and sea level allowances for Norway. *J. Mar. Sci. Eng.* **5**, <https://doi.org/10.3390/jmse5030036> (2017).
57. Luik, K. et al. Development shifts on the emerging Jarve coast (Estonia) in late Holocene. *Mar. Geol.* **481**, <https://doi.org/10.1016/j.margeo.2025.107478> (2025).
58. Sigmundsson, F. et al. Geodynamics of Iceland and the signatures of plate spreading. *J. Volcanol. Geotherm. Res.* **391**, <https://doi.org/10.1016/j.jvolgeores.2018.08.014> (2020).
59. Keiding, M., Arnadóttir, T., Jónsson, S., Deciem, J. & Hooper, A. Plate boundary deformation and man-made subsidence around geothermal fields on the Reykjanes Peninsula, Iceland. *J. Volcanol. Geotherm. Res.* **194**, 139–149 (2010).
60. Cao, Y. M., Jónsson, S. & Hreinsdóttir, S. Iceland kinematics from InSAR. *J. Geophys. Res. Solid Earth* **128**, <https://doi.org/10.1029/2022jb025546> (2023).
61. Bianco, L. Petrological, mineralogical and geochemical characteristics of the globigerina limestone outcropping at Fomm Ir-Rih, Malta. *C. R. De. L Acad. Bulg. Des. Sci.* **73**, 985–991 (2020).
62. Kakar, N., Popovski, V. & Robinson, N. A. *Fulfilling the Sustainable Development Goals* (Routledge, 2022).
63. Lewis, N. *National Security and Human Health Implications of Climate Change* 13–24 (Springer, 2011).
64. Kirwan, M. L. & Gedan, K. B. Sea-level driven land conversion and the formation of ghost forests. *Nat. Clim. Change* **9**, 450–457 (2019).
65. Smart, L. S. et al. Aboveground carbon loss associated with the spread of ghost forests as sea levels rise. *Environ. Res. Lett.* **15**, <https://doi.org/10.1088/1748-9326/aba136> (2020).
66. Biondic, R., Plantak, L., Radovan, A. M. & Measki, H. Saltwater intrusion of coastal Karstic aquifer on the example of the Boljkovac water supply pumping station near Zadar, Croatia. *Quaternary* **5**, <https://doi.org/10.3390/quat5030036> (2022).
67. Scarascia, M. E. V., di, Battista, F. & Salvati, L. Water resources in Italy: availability and agricultural uses. *Irrigation Drain.* **55**, 115–127 (2006).
68. Burri, E. & Petitta, M. Agricultural changes affecting water availability: from abundance to scarcity (Fucino plain, central Italy). *Irrigation Drain.* **53**, 287–299 (2004).
69. Jodar-Abellan, A., López-Ortiz, M. I. & Melgarejo-Moreno, J. Wastewater treatment and water reuse in Spain. Current situation and perspectives. *Water* **11**, <https://doi.org/10.3390/w11081551> (2019).
70. Chaussard, E., Amelung, F., Abidin, H. & Hong, S. H. Sinking cities in Indonesia: ALOS PALSAR detects rapid subsidence due to groundwater and gas extraction. *Remote Sens. Environ.* **128**, 150–161 (2013).
71. Iglesias, A. & Garrote, L. Adaptation strategies for agricultural water management under climate change in Europe. *Agric. Water Manag.* **155**, 113–124 (2015).
72. Terranova, C., Ventura, G. & Vilaro, G. Multiple causes of ground deformation in the Napoli metropolitan area (Italy) from integrated persistent scatterers DInSAR, geological, hydrological, and urban infrastructure data. *Earth Sci. Rev.* **146**, 105–119 (2015).
73. Törnqvist, T. E. et al. Mississippi delta subsidence primarily caused by compaction of Holocene strata. *Nat. Geosci.* **1**, 173–176 (2008).
74. Yildirim, E. & Demir, I. Agricultural flood vulnerability assessment and risk quantification in Iowa. *Sci. Total Environ.* **826**, <https://doi.org/10.1016/j.scitotenv.2022.154165> (2022).
75. Sultana, F. Critical climate justice. *The Geogr. J.* **188**, <https://doi.org/10.1111/geoj.12417> (2021).
76. Drakes, O. & Tate, E. Social vulnerability in a multi-hazard context: a systematic review. *Environ. Res. Lett.* **17**, 033001 (2022).

77. European Environment Agency. Just Resilience: Key EU actions on climate adaptation. Climate-ADAPT, 2022. Available at: https://climate-adapt.eea.europa.eu/en/eu-adaptation-policy/key-eu-actions/just-resilience/index_html.
78. Council of Europe. Strategic Action Plan for Roma and Traveller Inclusion 2020–2025. Document Ref. 117220GBR, 2020. Available at: <https://edoc.coe.int/en/roma-and-travellers/8508-council-of-europe-strategic-action-plan-for-roma-and-traveller-inclusion-2020-2025.html>.
79. European Union Agency for Fundamental Rights (FRA). Roma in 10 European Countries – Main results. Vienna, 25 October 2022. Available at: <https://fra.europa.eu/en/publication/2022/roma-survey-findings>.
80. Mycoo, M. A. Autonomous household responses and urban governance capacity building for climate change adaptation: Georgetown, Guyana. *Urban Clim.* **9**, 134–154 (2014).
81. Majumdar, R. & Weber, E. U. Multilevel intergroup conflict at the core of climate (in)justice: psychological challenges and ways forward. *Wiley Interdiscip. Rev. Clim. Change* **14**, <https://doi.org/10.1002/wcc.836> (2023).
82. Bilham, R. The seismic future of cities. *Bull. Earthq. Eng.* **7**, 839–887 (2009).
83. World Health Organization. *Community Health Insurance*, <<https://www.who.int/zh/news-room/fact-sheets/detail/community-based-health-insurance-2020>> (2020).
84. Shi, H. & Singh, A. Status and interconnections of selected environmental issues in the global coastal zones. *AMBIO A J. Hum. Environ.* **32**, 145–152 (2003).
85. Miller, M. M. & Shirzaei, M. Assessment of future flood hazards for southeastern Texas: synthesizing subsidence, sea-level rise, and storm surge scenarios. *Geophys. Res. Lett.* **48**, <https://doi.org/10.1029/2021gl092544> (2021).
86. Hinkel, J., Nicholls, R. J., Vafeidis, A. T., Tol, R. S. J. & Avagianou, T. Assessing risk of and adaptation to sea-level rise in the European Union: an application of DIVA. *Mitig. Adapt. Strateg. Glob. Change* **15**, 703–719 (2010).
87. Vernimmen, R. & Hooijer, A. New LiDAR-based elevation model shows greatest increase in global coastal exposure to flooding to be caused by early-stage sea-level rise. *Earth's Future* **11**, <https://doi.org/10.1029/2022ef002880> (2023).
88. Holgate, S. J. et al. New data systems and products at the permanent service for mean sea level. *J. Coast. Res.* **29**, 493–504 (2013).
89. Wang, X., Meng, X. & Long, Y. Projecting 1 km-grid population distributions from 2020 to 2100 globally under shared socioeconomic pathways. *Sci. Data* **9**, 563 (2022).
90. Che, Y. et al. 3D-GloBFP: the first global three-dimensional building footprint dataset. *Earth Syst. Sci. Data Discuss.* **16**, 18 (2024).
91. Department, S. R. *Average transaction price of a new dwelling in Europe in 2023, by country*, <https://www.statista.com/statistics/868129/average-transaction-price-of-new-dwelling-europe/> (2023).
92. United Nations Department of Economic Social Affairs Population Division. *World Population Prospects 2024*, <https://population.un.org/wpp/downloads> (2024).
93. Fundación Secretariado Gitano & Daleph. *Estudio-Mapa sobre Vivienda y Población Gitana*, 2015. Madrid: Ministerio de Sanidad, Servicios Sociales e Igualdad, 2016. Available at: https://www.gitanos.org/centro_documentacion/estudios/estudio_mapa_sobre_vivienda_y_poblacion_gitana_2015/.
94. Murakami, D., Yoshida, T. & Yamagata, Y. Gridded GDP projections compatible with the five SSPs (shared socioeconomic pathways). *Front. Built Environ.* **7**, 760306 (2021).

Acknowledgements

We are grateful to Dr. Olusegun Dada and Dr. Alireza Bahadori for handling the editorial process of the manuscript and to the anonymous reviewers for their constructive comments, which greatly helped to improve the quality of the article. The work by Huilin Chen, Chisheng Wang, Huawei Hou, and Qingquan Li has been supported by the National Natural Science Foundation of China (42374018), the Guangdong Basic and Applied Basic Research Foundation (2025B1515020092), the Disciplines Breakthrough Project in Aerospace Information and Spatiotemporal Intelligence, MOE China, and the Shenzhen Science and Technology Program (KCXFZ20240903093000002 and SYSPG20241211173845013). Research by J.F. has been supported by grant G2HOTSPOTS (PID2021-122142OBI00) from the AEI/10.13039/501100011033/Union EuropeaNextGenerationEU/PRTR.

Author contributions

H.C. and C.W. conceived and designed the study. H.C. collected the data, performed the analysis, and drafted the initial manuscript. J.F., H.H., L.C., and Q.L. revised the manuscript. C.W. supervised the project, provided funding, and reviewed and edited the manuscript. All authors contributed to the interpretation of the results.

Competing interests

The authors declare no competing interests.

Additional information

Supplementary information The online version contains supplementary material available at <https://doi.org/10.1038/s43247-026-03190-y>.

Correspondence and requests for materials should be addressed to Chisheng Wang.

Peer review information *Communications Earth and Environment* thanks the anonymous reviewers for their contribution to the peer review of this work. Primary handling editors: Olusegun Dada and Alireza Bahadori. A peer review file is available.

Reprints and permissions information is available at <http://www.nature.com/reprints>

Publisher's note Springer Nature remains neutral with regard to jurisdictional claims in published maps and institutional affiliations.

Open Access This article is licensed under a Creative Commons Attribution-NonCommercial-NoDerivatives 4.0 International License, which permits any non-commercial use, sharing, distribution and reproduction in any medium or format, as long as you give appropriate credit to the original author(s) and the source, provide a link to the Creative Commons licence, and indicate if you modified the licensed material. You do not have permission under this licence to share adapted material derived from this article or parts of it. The images or other third party material in this article are included in the article's Creative Commons licence, unless indicated otherwise in a credit line to the material. If material is not included in the article's Creative Commons licence and your intended use is not permitted by statutory regulation or exceeds the permitted use, you will need to obtain permission directly from the copyright holder. To view a copy of this licence, visit <http://creativecommons.org/licenses/by-nc-nd/4.0/>.

© The Author(s) 2026